

X-ray analysis of JWST's first galaxy cluster lens SMACS J0723.3-7327

A. Liu^{*}, E. Bulbul, M. E. Ramos-Ceja, J. S. Sanders, V. Ghirardini, Y. E. Bahar, M. Yeung, E. Gattuzz, M. Freyberg,
C. Garrel, X. Zhang, A. Merloni, K. Nandra

Max Planck Institute for Extraterrestrial Physics, Giessenbachstrasse 1, 85748 Garching, Germany

October 4, 2022

ABSTRACT

Context. SMACS J0723.3-7327 is the first galaxy cluster lens observed by *JWST*. Based on the Early Release Observation data from *JWST*, several groups have reported the results on strong lensing analysis and mass distribution of this cluster. The new lens model dramatically improves upon previous results, thanks to the unprecedented sensitivity and angular resolution of *JWST*. However, limited by the angular coverage of the *JWST* data, the strong lensing models only cover the central region. X-ray analysis on the hot ICM is necessary to obtain a more complete constraint on the mass distribution in this very massive cluster.

Aims. In this work, we aim to perform a comprehensive X-ray analysis of J0723 to obtain accurate ICM hydrostatic mass measurements, using the X-ray data from *SRG (Spectrum Roentgen Gamma)/eROSITA* and *Chandra* X-ray observatories. By comparing the hydrostatic mass profile with the strong lensing model, we aim to provide the most reliable constraint on the distribution of mass up to R_{500} .

Methods. Thanks to the *eROSITA* all-sky survey and *Chandra* data, which provide high S/N and high angular resolution respectively, we are able to constrain the ICM gas density profile and temperature profile with good accuracy both in the core and to the outskirts. With the density and temperature profiles, we compute the hydrostatic mass profile, which is then projected along the line of sight to compare with the mass distribution obtained from the recent strong lensing analysis based on *JWST* data. We also deproject the strong lensing mass distribution using the hydrostatic mass profile we obtained in this work.

Results. The X-ray results obtained from *eROSITA* and *Chandra* agree very well with each other. The hydrostatic mass profiles we measured in this work, both projected and deprojected, are in good agreement with recent strong lensing results based on *JWST* data, at all radii. The projected hydrostatic mass within 128 kpc (the estimated Einstein radius) is $(8.1 \pm 0.7) \times 10^{13} M_{\odot}$, consistent with the strong lensing mass reported in [Caminha et al. \(2022\)](#): $(8.6 \pm 0.2) \times 10^{13} M_{\odot}$, and in [Mahler et al. \(2022\)](#): $(7.6 \pm 0.2) \times 10^{13} M_{\odot}$. With the hydrostatic mass profile, we measured $R_{2500} = 0.54 \pm 0.04$ Mpc and $M_{2500} = (3.5 \pm 0.8) \times 10^{14} M_{\odot}$, while the R_{500} and M_{500} are 1.33 ± 0.23 Mpc and $(10.2 \pm 5.3) \times 10^{14} M_{\odot}$, with relatively larger error bar due to the rapidly decreasing S/N in the outskirts.

Key words. galaxies: clusters: intracluster medium – galaxies: clusters: individual: SMACS J0723.3-7327 – X-rays: galaxies: clusters

1. Introduction

Mass and mass distribution in massive galaxy clusters are crucial to study the property of dark matter halos and the evolution of the large-scale structures in the Universe. There are several independent ways to measure the mass distribution of clusters, such as strong/weak gravitational lensing effect of background sources (see, e.g., [Kneib & Natarajan 2011](#); [Umetsu 2020](#); [Caminha et al. 2017](#); [Bergamini et al. 2022](#)), velocity dispersion of member galaxies (e.g., [Girardi et al. 1993](#)), and hydrostatic equilibrium of the X-ray emitting intracluster medium (ICM) (e.g., [Ettori et al. 2013](#); [Ghirardini et al. 2018](#); [Ettori et al. 2019](#)). Among them, the X-ray hydrostatic mass has the unique advantage of acquiring the deprojected mass distribution, while the other methods can only measure the line-of-sight integrated mass. Another difference in these methods is that they are sensitive in different radial ranges. For example, strong lensing has the most prominent effect near the critical line (close to the core region, usually smaller than $0.3R_{500}$), where ICM hydrostatic mass may suffer from bias due to non-gravitational effects such as radiative cooling and AGN feedback particularly when a strong cool core ex-

ists, and non-thermal pressure due to gas turbulence or bulk motions. Therefore, it is important to have the mass distribution in galaxy clusters measured from multiple independent methods, to understand the biases in each of them.

In this work, we will focus on a specific target, SMACS J0723.3-7327 (hereafter J0723), a massive galaxy cluster at redshift 0.39 ([Ebeling et al. 2001](#)). J0723 (R.A. = 7:23:19.20, Dec. = -73:27:22.5) was identified as a galaxy cluster in the southern extension of the Massive Cluster Survey (MACS; [Ebeling et al. 2001](#)). It was also detected in X-ray band in the *ROSAT* All-Sky Survey (RASS; [Voges et al. 1999](#)), and in Sunyaev-Zeldovich survey by *Planck* ([Planck Collaboration et al. 2014](#); [Planck Collaboration et al. 2016a](#)). J0723 is the first galaxy cluster lens observed by the James Webb Space Telescope (*JWST*). Based on the Early Release Observation data from *JWST*, several groups have reported the results on strong lensing analysis and mass distribution of this cluster ([Mahler et al. 2022](#); [Caminha et al. 2022](#)). The new lens model dramatically improves upon previous results, thanks to the unprecedented sensitivity and angular resolution of *JWST*, which lead to the discovery of significantly more multiple images and lensed sources. However, the *JWST* observation only covers the core of

* e-mail: liuang@mpe.mpg.de

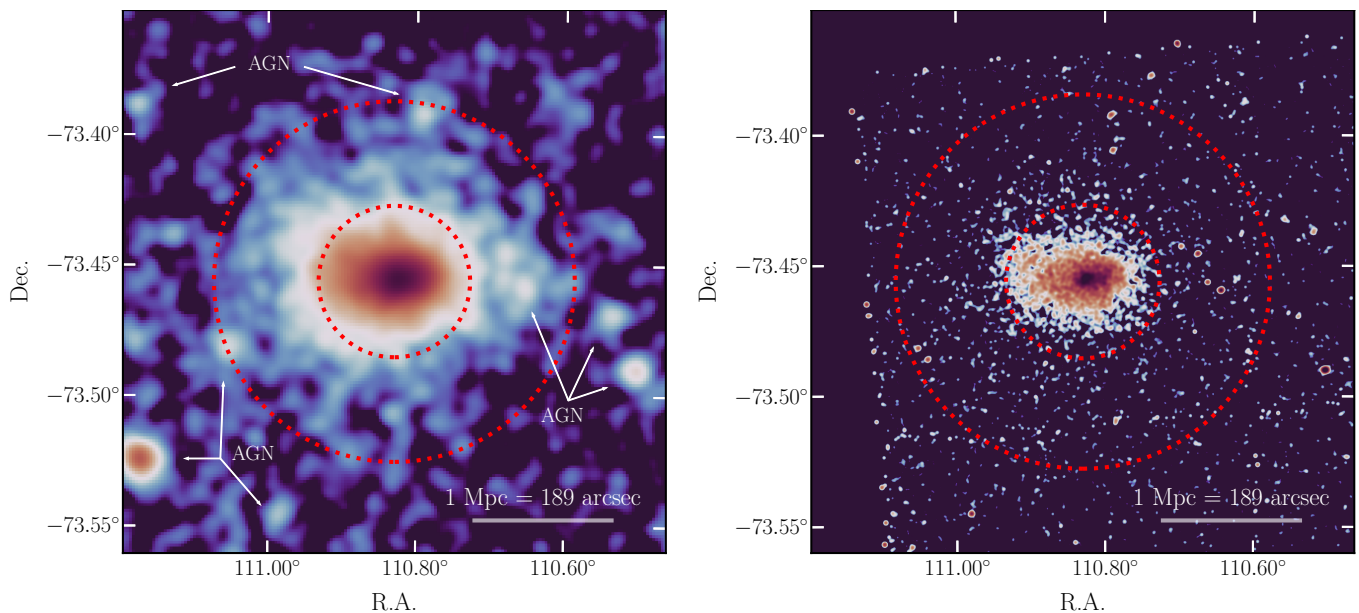


Fig. 1. X-ray image of J0723. *Left panel:* *eROSITA* exposure-corrected image in the 0.2–2.3 keV band, smoothed with a Gaussian of $\sigma = 10''$. *Right panel:* *Chandra* exposure-corrected image in the 0.5–7 keV band, smoothed with a Gaussian of $\sigma = 2''$. The images are centered at the coordinate (R.A. = 7:23:19.20, Dec. = -73:27:22.5). The large and small red circles show the positions of $R_{500}=1.33$ Mpc and $R_{2500}=0.54$ Mpc, determined from the hydrostatic mass profile (R_{500}/R_{2500} is the radius within which the average density is 500/2500 times the critical density at cluster’s redshift, see Sect. 3). On the *eROSITA* image, the emission of the cluster clearly extends to $\sim R_{500}$. On the *Chandra* image, the emission only slightly exceeds R_{2500} , but the cluster core is better resolved. The red point sources on the *Chandra* image (visible as larger white sources on the *eROSITA* image due to the larger PSF) are AGN which are masked in the analysis. Some bright point sources are marked on the *eROSITA* image.

the cluster, which limits the strong lensing analysis to the central ~ 200 kpc (Caminha et al. 2022), despite that Mahler et al. (2022) extrapolated the model to ~ 1 Mpc. Since the strong lensing effect is only sensitive to the projected mass, the small coverage of the strong lensing model implies that, with the strong lensing results only, the mass distribution in cluster outskirts is unknown, hence one cannot get the true/deprojected mass distribution in cluster center. Therefore, to obtain a more complete constraint on the mass distribution in J0723, the strong lensing model needs to be combined with other probes such as ICM hydrostatic analysis, which provides constraints on the mass distribution from the center to the outskirts.

J0723 has been observed in the X-ray band by *Chandra* and *XMM-Newton*. Using the archival data of *XMM-Newton*, Lovisari et al. (2020) measured the hydrostatic mass of J0723, but with only three bins in the temperature profile. Their results show that J0723 is massive ($M_{500} = 10.10^{+1.57}_{-1.23} \times 10^{14} M_{\odot}$) and hot ($kT_{500} = 7.53^{+0.53}_{-0.53}$ keV). J0723 is also observed by *eROSITA* during its survey observation phase. In this work, we will perform an X-ray study on J0723 based on the *eROSITA* all-sky survey data, aiming at providing the projected and deprojected hydrostatic mass profiles, to the largest extent allowed by the data. Due to the relatively low angular resolution of *eROSITA* (FOV averaged half energy width HEW $\sim 30''$ – $35''$ over the soft band), we will also leverage the high angular resolution of the archival *Chandra* data to constrain the temperature profile in cluster center. On the other hand, the archival *Chandra* data is too shallow to constrain gas properties in cluster outskirts (see Fig. 1). The *eROSITA* all-sky survey data, thanks to its large effective area in soft energies, is most sensitive to low temperature gas at cluster outskirts (~ 1400 cm 2 at 1 keV). Therefore, it will play a crucial role to determine the gas density and temperature profiles

up to $\sim R_{500}$, which are key information in the conversion between projected and deprojected mass profiles. The results in this work will also be helpful to further verify the performance of *eROSITA*, improving our understanding of the calibration systematics in the analysis of *eROSITA* survey-mode data on very hot clusters (~ 10 keV for J0723).

The paper is organized as follows. In Sect. 2, we introduce the *eROSITA* and *Chandra* X-ray datasets we used in this work and the reduction of these data. In Sect. 3, we present the X-ray data analysis, including the spectral and image fitting, and the computation of the mass profile. In Sect. 4, we discuss our results and possible caveats in our analysis. Our conclusions are summarized in Sect. 5. Throughout this paper, we adopt the concordance Λ CDM cosmology with $\Omega_{\Lambda} = 0.7$, $\Omega_{\text{m}} = 0.3$, and $H_0 = 70$ km s $^{-1}$ Mpc $^{-1}$. At redshift $z = 0.39$, 1 arcsec corresponds to 5.29 kpc. The solar abundance table from Asplund et al. (2009) is adopted. X-ray spectral fitting in this work is done with Xspec version 12.11.1 (Arnaud 1996) using C-statistics (Cash 1979). Quoted error bars correspond to a 1σ confidence level unless noted otherwise.

2. X-ray data reduction

In this work, we used the X-ray data from *eROSITA* and *Chandra*. The *eROSITA* data are obtained during the all-sky survey (eRASS) from December 2019 to February 2022. J0723 was scanned five times in the first five all-sky surveys (eRASS:5). The total effective exposure after correcting for vignetting effect is ~ 4.4 ks. We note that the exposure on J0723 is significantly larger than the average depth of eRASS, because it lies close to the south ecliptic pole of the survey. The *Chandra* observation

(ObsID: 15296, PI: S. Murray) was performed in April 2014, with a cleaned exposure time of 16.5 ks.

2.1. eROSITA

The eRASS:5 data are processed with the eROSITA Science Analysis Software System (eSASS, Brunner et al. 2022)¹. For all the seven telescope modules (TMs), we apply pattern recognition and energy calibration to produce calibrated event lists. In comparison with the data processing c001 from the eROSITA Early Data Release², the data processing we performed in this work has an improved low energy detector noise suppression, and a better computation of the subpixel position. The event lists are further filtered after the determination of good time intervals, dead times, corrupted events and frames, and bad pixels. Using star-tracker and gyro data, celestial coordinates are assigned to the reconstructed X-ray photons, which can then be projected into the sky to produce images and exposure maps. All valid pixel patterns are selected in this work, i.e., single, double, triple, and quadruple events. The vignetting and point spread function (PSF) calibrations are less accurate in the corners of CCDs, therefore we use only photons which are detected at off-axis angles ≤ 30 arcmin. The soft band of TMs 5 and 7 are affected by light leak (Predehl et al. 2021), therefore we ignored the events below 1 keV of TMs 5 and 7 in our analysis. Point sources are detected in the eROSITA soft band (0.2–2.3 keV) image using the same method described in Brunner et al. (2022), and are masked from the analysis. We also include the point source list as detected by *Chandra*. The radius of the masked point source has the minimum value of $30''$, slightly larger than the half-energy width of eROSITA’s FOV-averaged PSF ($26''$). For several bright point sources, the radius was increased manually to mask the residual emission due to the outer wings of the PSF. We checked the masked regions visually and confirmed that after masking, the residual contamination from point sources is negligible.

2.2. Chandra

The reduction of *Chandra* data is performed using the software CIAO v4.14, with the latest release of the *Chandra* Calibration Database at the time of writing (CALDB v4.9). Time intervals with a high background level are filtered out by performing a 2σ clipping of the light curve in the 2.3–7.3 keV band source-free image. The total cleaned exposure time after deflare is ~ 16.5 ks.

Point sources within the field of view (FOV) were identified with wavdetect on the *Chandra* 0.5–7 keV band image, checked visually, and eventually masked. Gaps between the CCD chips are also masked.

The eROSITA and *Chandra* images of J0723 are shown in Fig. 1. We note that, while the ICM emission in cluster outskirts can be well detected by the eROSITA data, it is beyond the flux limit of the *Chandra* data, despite that the *Chandra* data will also play an important role in constraining the ICM properties in the core. Therefore, in the following analysis, we will consider the *Chandra* results in the outskirts ($> \sim 600$ kpc) as an extrapolation, and rely on the eROSITA measurements in these regions.

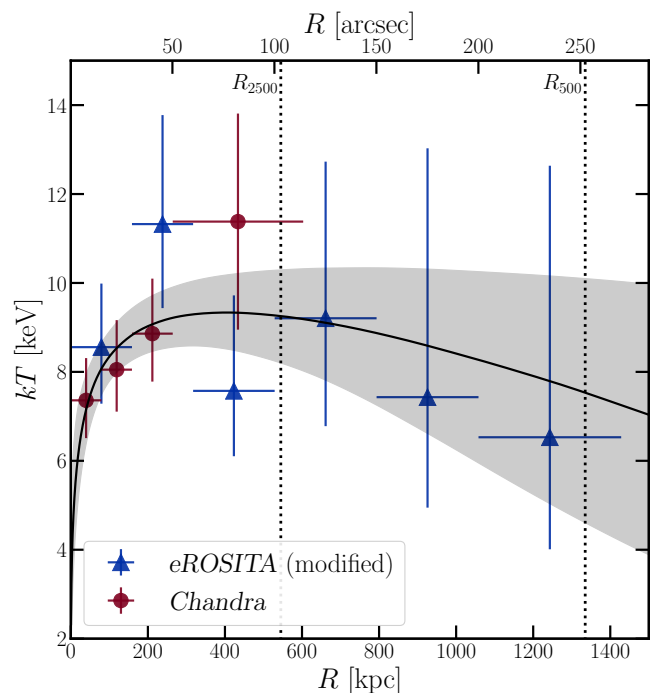


Fig. 2. Temperature profile of J0723. Blue and red data points are from the analysis of eROSITA (after modification using hard-band results) and *Chandra*, respectively. The solid black curve and shaded area are the best-fit model of the profile. The two dotted lines indicate the positions of $R_{500}=1.33$ Mpc and $R_{2500}=0.54$ Mpc, determined from the hydrostatic mass profile measured by eROSITA (the blue line in Fig. 5, see Sect. 3.3, same for the other figures).

3. X-ray data analysis

In this section, we will introduce our X-ray analysis for both eROSITA and *Chandra*. We perform spectral analysis to measure the gas temperature profile, and imaging analysis to measure the gas density. The mass profile is then derived from the temperature and density profiles using the hydrostatic equilibrium equation.

3.1. Spectral analysis

3.1.1. eROSITA

For the spectral analysis of eROSITA, we choose six annuli whose outer radii are $30''$, $60''$, $100''$, $150''$, $200''$, and $270''$. The center of the regions is R.A. = 7:23:19.20, Dec. = $-73:27:22.5$, determined by fitting the *Chandra* image (see Sect. 3.2 and Fig. 1). The spectral extraction and the computing of ancillary response files (ARFs), and redistribution matrix files (RMFs) from the seven telescope modules are performed using the eSASS algorithm srctool. The background spectrum is extracted from a concentric annulus with inner and outer radii of 3.5 Mpc and 5 Mpc, far beyond the emission of the ICM. Fitting of the background spectrum is done using the similar approach described in Liu et al. (2022). The instrumental background due to the interactions of high-energy particles with the telescope and the satellite is obtained by fitting the filter-wheel-closed (FWC) data with a broken power-law and a series of Gaussian lines (Freyberg et al. 2020). We use the best fitting parameters obtained from the FWC data to fit the local background, but allowing a

¹ version eSASSusers_211214_0_4.

² <https://erosita.mpe.mpg.de/edr/>

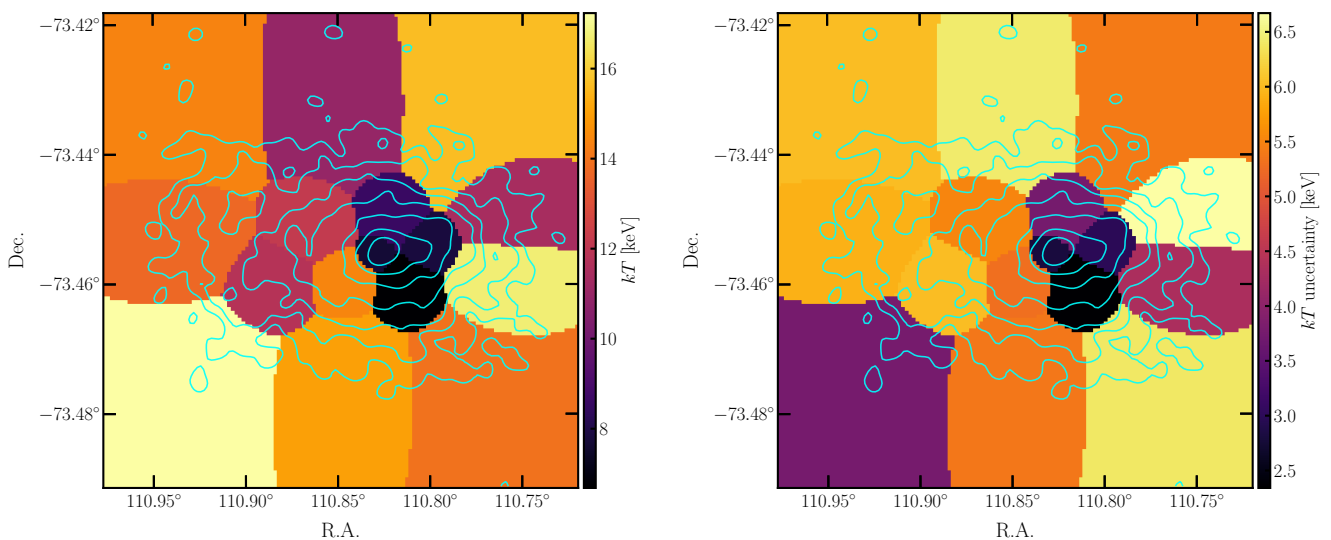


Fig. 3. ICM temperature distribution measured with *Chandra* data. The left panel and right panel show maps of temperature and 1σ uncertainty, respectively. The contours colored in cyan are generated from the 0.5–7 keV *Chandra* image.

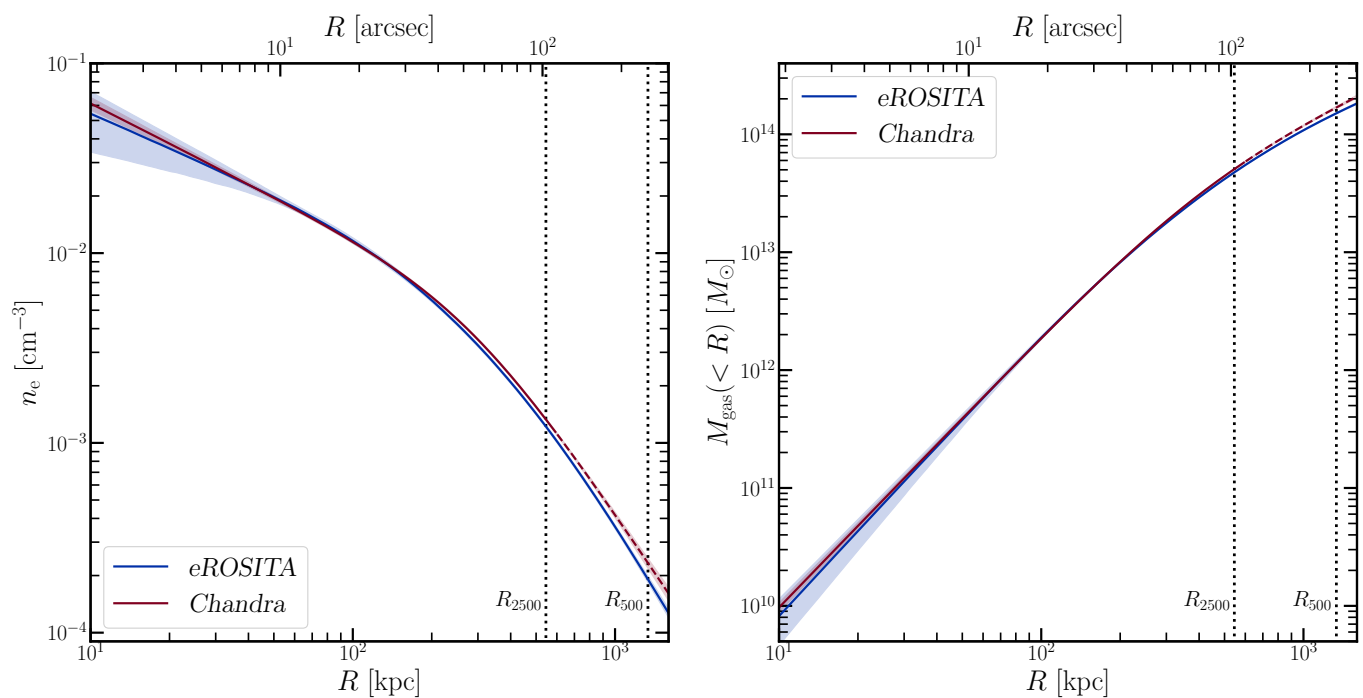


Fig. 4. Results of X-ray imaging analysis from *eROSITA* and *Chandra* using MBProj2D. *Left panel:* Electron density profiles. *Right panel:* Gas mass profiles. The *Chandra* results above 0.6 Mpc are plotted as dashed lines.

free overall normalisation. The cosmic X-ray background (CXB) is modeled by considering the contribution from the Local Hot Bubble (e.g., Snowden et al. 2008; Kuntz & Snowden 2000), the Galactic Halo, and unresolved point sources. The Local Hot Bubble and the Galactic Halo are modeled by an unabsorbed and absorbed `apec` (Smith et al. 2001; Foster et al. 2012), and the emission due to unresolved sources is modeled by an absorbed `powerlaw`, where the index is frozen to 1.46 (see, e.g., Luo et al. 2017). The Galactic hydrogen absorption is modeled using `tbabs` (Wilms et al. 2000), where the hydrogen column density n_{H} is fixed to $22.5 \times 10^{20} \text{ cm}^{-2}$, according to the $n_{\text{H,tot}}$

value provided by Willingale et al. (2013). Therefore, our final CXB model is: `apec+tbabs(apec+powerlaw)`. The ICM emission is modeled with a single `apec` model, where the redshift is fixed at 0.39, metal abundance is fixed at 0.3. We do not make any attempt to measure the chemical property of the ICM in this work, as the metallicity of massive clusters is very well constrained from cluster center (e.g., Liu et al. 2018, 2020) to outskirts (e.g., Mernier et al. 2018; Ezer et al. 2017; Bulbul et al. 2016; Simionescu et al. 2017), and line emission is negligible in a hot cluster like J0723.

Table 1. Temperature profile measured by *eROSITA* before and after the hard-band modification.

Region	kT (full-band) [keV]	kT (modified) [keV]
0''–30''	$4.54^{+0.52}_{-0.49}$	$8.56^{+1.43}_{-1.27}$
30''–60''	$5.54^{+0.82}_{-0.67}$	$11.32^{+2.45}_{-1.89}$
60''–100''	$4.17^{+0.80}_{-0.59}$	$7.57^{+2.15}_{-1.47}$
100''–150''	$4.78^{+1.23}_{-0.93}$	$9.21^{+3.52}_{-2.43}$
150''–200''	$4.11^{+2.00}_{-1.03}$	$7.43^{+5.60}_{-2.48}$
200''–270''	$3.75^{+2.23}_{-1.09}$	$6.53^{+6.11}_{-2.52}$

A common issue in a combined analysis of clusters using the data from multiple telescopes is the discrepancy in the temperatures measured by different instruments. For example, Schellenberger et al. (2015) find that the cluster temperatures measured by *XMM-Newton/EPIC* are significantly lower than *Chandra/ACIS*. They also find that the difference is mostly due to the discrepancy in the cross-calibration in the soft band, and the temperatures measured only using the hard band are more consistent.

Therefore, in the *eROSITA* analysis, we adopt the temperatures constrained from the hard band spectra (2–8 keV). Given the low number of counts we have for J0723, we are not able to perform hard-band fitting for all the bins in the temperature profile. However, this bias is systematic, and we can simply get a conversion factor: $f_T \equiv \ln T_{\text{hard}} / \ln T_{\text{full}}$, from a high S/N spectrum, and apply this conversion to the T_{full} of the spectrum with lower S/N, where T_{hard} cannot be constrained. To obtain the conversion factor f_T , we extract the spectrum within 2 arcmin to make sure the spectrum has a high S/N, and fit the full band (0.5–8 keV) and hard band (2–8 keV) spectra respectively. The best-fit temperatures are $T_{\text{hard}} = 9.03^{+5.40}_{-2.60}$ keV and $T_{\text{full}} = 4.72^{+0.36}_{-0.32}$ keV. Therefore, we have $f_T = 1.417$. It should be noted that, since we assume a systematic conversion between T_{hard} and T_{full} , we ignore the statistical uncertainties of T_{hard} and T_{full} in the computation of f_T , but only use the best-fit values. As a comparison, we also measured the temperature with *Chandra* for the same region, and the result is $T_{\text{Chandra}} = 9.01^{+0.60}_{-0.56}$ keV, in very good agreement with the *eROSITA* hard band result. In Table 1, we list the temperature values in each bin by fitting the full band, and the modified values using the above strategy.

The modified temperature profile we obtained from the *eROSITA* data is plotted in Fig. 2. We note that the two innermost bins only have widths of 30'', thus the spectra are unavoidably affected by PSF spilling of the adjacent bin. However, this effect should be no more than a slight smoothing of the profile. We stress that in these regions we have *Chandra* data with better resolution, thus the contribution of the *eROSITA* temperature profile is more significant in the outskirts. Therefore the impact of PSF spilling can be safely ignored in these regions.

3.1.2. Chandra

For the spectral analysis of *Chandra* data, we increased the spatial resolution of the temperature profile in the central region ($R < 50''$) with respect to the *eROSITA* result. The ARF and RMF of each spectrum were computed with the commands `mkarf` and `mkacisrmf`. The background spectra were extracted from the ‘blank sky’ files, and processed using the `blanksky` script (we used the default options with `weight_method` ‘particle’ and `bkgparams` = [energy = 9000:12000]). We used the full energy range (0.5–7 keV) for the fit. We also did the

same analysis by using only the hard band (2–7 keV) as we did for *eROSITA*. However, we find no significant difference between the T_{hard} and T_{full} for *Chandra*. This is probably because of the much smaller effective area of *Chandra* in the soft band, which does not contribute much to the fit. We, therefore, adopted the full band fitting results for *Chandra*. The temperature profile from *Chandra* data is plotted in Fig. 2.

Using *Chandra* data, we also perform a spatially-resolved spectral analysis to measure the 2D distribution of temperature, to search for any peculiar structure and inspect the consistency with the 1D profile. The regions for the 2D analysis are selected using the Voronoi tessellations method (Cappellari & Copin 2003). Each region contains ~ 300 net counts in the energy range 0.5–7 keV. The temperature map and its uncertainty are shown in Fig. 3. We find that the 1D temperature file is in broad consistent with the 2D map. A clear cool core at ~ 7 keV can be observed in the temperature map, in accordance with the temperature profile.

3.1.3. Combined temperature profile

In general, the results of *eROSITA* and *Chandra* agree well with each other, particularly in the central regions. In the outskirts, both datasets have large error bars. J0723 hosts a weak cool core, with $T_{\text{core}} \sim 7$ keV and $T_{\text{max}} \sim 10$ keV. Considering that the temperature variance within our datasets is less than a factor of 2, the difference between projected and deprojected temperature profiles is expected to be rather small, well below the statistical uncertainty. Therefore, we do not make any attempt to deproject the temperature profile.

The *eROSITA* and *Chandra* combined temperature profile is fit with the model presented in Vikhlinin et al. (2006), in order to get a smooth temperature profile:

$$T(r) = T_0 \cdot \frac{(r/r_{\text{cool}})^{a_{\text{cool}}} + T_{\text{min}}/T_0}{(r/r_{\text{cool}})^{a_{\text{cool}}} + 1} \cdot \frac{(r/r_i)^{-a}}{[1 + (r/r_i)^b]^{c/b}}. \quad (1)$$

The fitting is done using the MCMC tool of Foreman-Mackey et al. (2013). The best-fit profile is shown in Fig. 2.

3.2. Image fitting with MBProj2D

To measure the gas density profile, we perform imaging analysis using the MultiBand Projector 2D (MBProj2D) tool³. MBProj2D (Sanders et al. 2018) is a code which forward-models background-included X-ray images of galaxy clusters to fit cluster and background emission simultaneously and measures the profiles of ICM properties including density, flux, luminosity, etc. By using a single band image, MBProj2D is only sensitive to the density of the ICM. By using multiple bands from soft to hard and given enough counts, MBProj2D is also able to model the temperature variation within the cluster. When sufficient energy bands are provided, MBProj2D can give equivalent results as expected from spatially-resolved spectral analysis, e.g., metallicity and temperature profiles of the ICM. By assuming hydrostatic equilibrium, MBProj2D can also measure hydrostatic mass profile. We refer the readers to Sanders et al. (2018) for more details about MBProj2D⁴.

In this work, since we already have the temperature profile from spectral analysis, we only use the basic function of MBProj2D, to measure the density profile using multiple band

³ <https://github.com/jeremysanders/mbproj2d>

⁴ <https://mbproj2d.readthedocs.io/en/latest/>

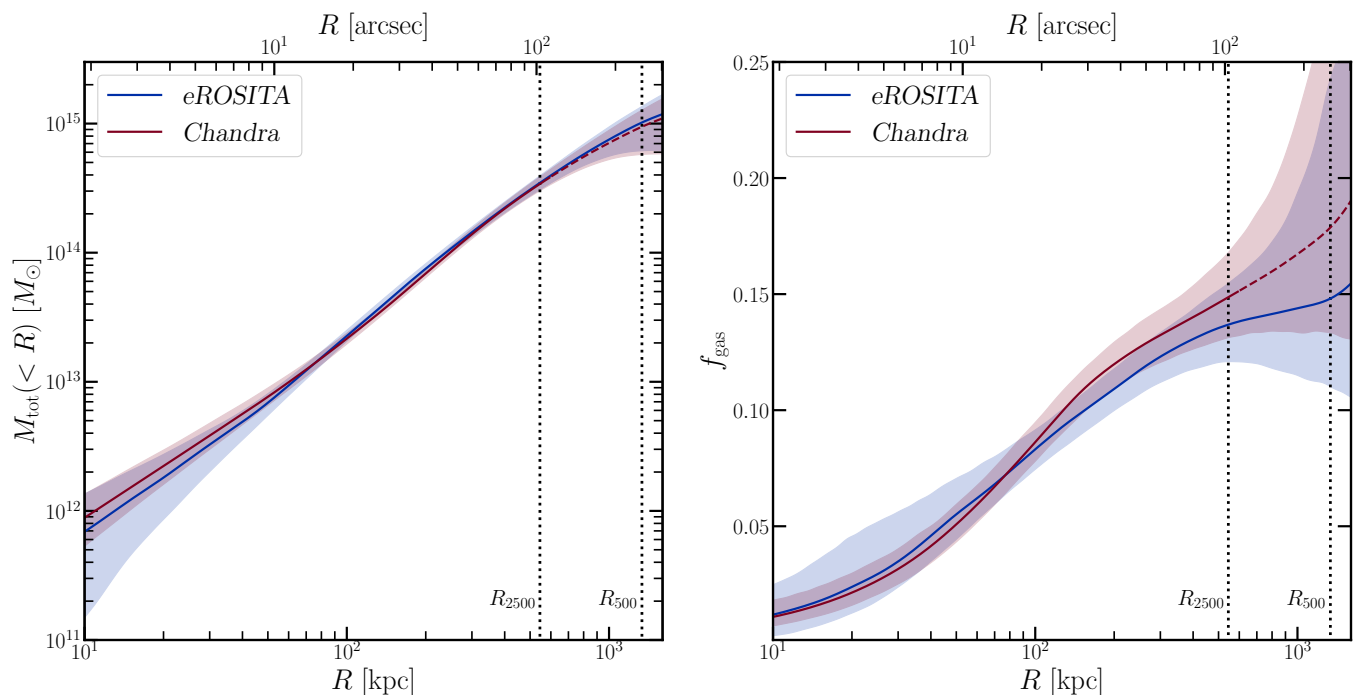


Fig. 5. Results of hydrostatic analysis. *Left panel:* hydrostatic mass profiles of J0723 using the best-fit model of the combined temperature profile (Fig. 2) and the density profile of *eROSITA* (blue) and *Chandra* (red). *Right panel:* gas mass fraction (f_{gas}) profiles. The two dotted lines indicate the positions of $R_{500}=1.33$ Mpc and $R_{2500}=0.54$ Mpc, determined from the hydrostatic mass profile measured by *eROSITA* (blue line in the left panel).

images, without assuming a hydrostatic mass model, and then derive the model-independent hydrostatic mass profile backwardly using the temperature and density profiles. For *eROSITA* data, we create images and exposure maps in the following energy bands (in units of keV): [0.3–0.6], [0.6–1.1], [1.1–1.6], [1.6–2.2], [2.2–3.5], [3.5–5.0], [5.0–7.0], using the `evtool` command in `eSASS`. The size of the image is 6 Mpc \times 6 Mpc, which is large enough to include the background. Point sources within the image are masked following the same approach in the spectral analysis. PSF and ARF variations across different bands are considered properly. The model of density profile is from [Vikhlinin et al. \(2006\)](#), but without the second β component:

$$n_p n_e = n_0^2 \cdot \frac{(r/r_c)^{-\alpha}}{(1+r^2/r_c^2)^{3\beta-\alpha/2}} \frac{1}{(1+r^\gamma/r_s^\gamma)^{\epsilon/\gamma}}, \quad (2)$$

where n_e and n_p are electron density and proton density, and we assume $n_e = 1.21n_p$. n_0 , r_c , α , β , γ , r_s and ϵ are free parameters.

A similar analysis was done also for the *Chandra* data. The following energy bands (in units of keV) are used for *Chandra* analysis: [0.5–0.75], [0.75–1.0], [1.0–1.25], [1.25–1.5], [1.5–2.0], [2.0–3.0], [3.0–4.0], [4.0–5.0], [5.0–6.0], [6.0–7.0]. Limited by the FOV of *Chandra*, the size of the image is reduced to 4 Mpc \times 4 Mpc. However, this is still large enough to contain the background emission in the fitting. The *Chandra* exposure map computed by CIAO is always folded by the effective area. In order to get the unfolded exposure map as required by MBProj2D, we extracted a spectrum in the center of the image and renormalised the folded exposure maps using the exposure time information of the spectrum.

The electron density profiles measured using MBProj2D are plotted in Fig. 4. Also shown are the cumulative gas mass profiles. The results from *eROSITA* and *Chandra* agree very well.

There is only a very small discrepancy in the density profile in the outskirts, which is acceptable considering that the *Chandra* data is too shallow in these regions, thus the *Chandra* result is probably an extrapolation of the best-fit model dominated by the central region.

3.3. Hydrostatic mass

With the ICM temperature profile and density profile, we derive the hydrostatic mass profile using the hydrostatic equilibrium equation:

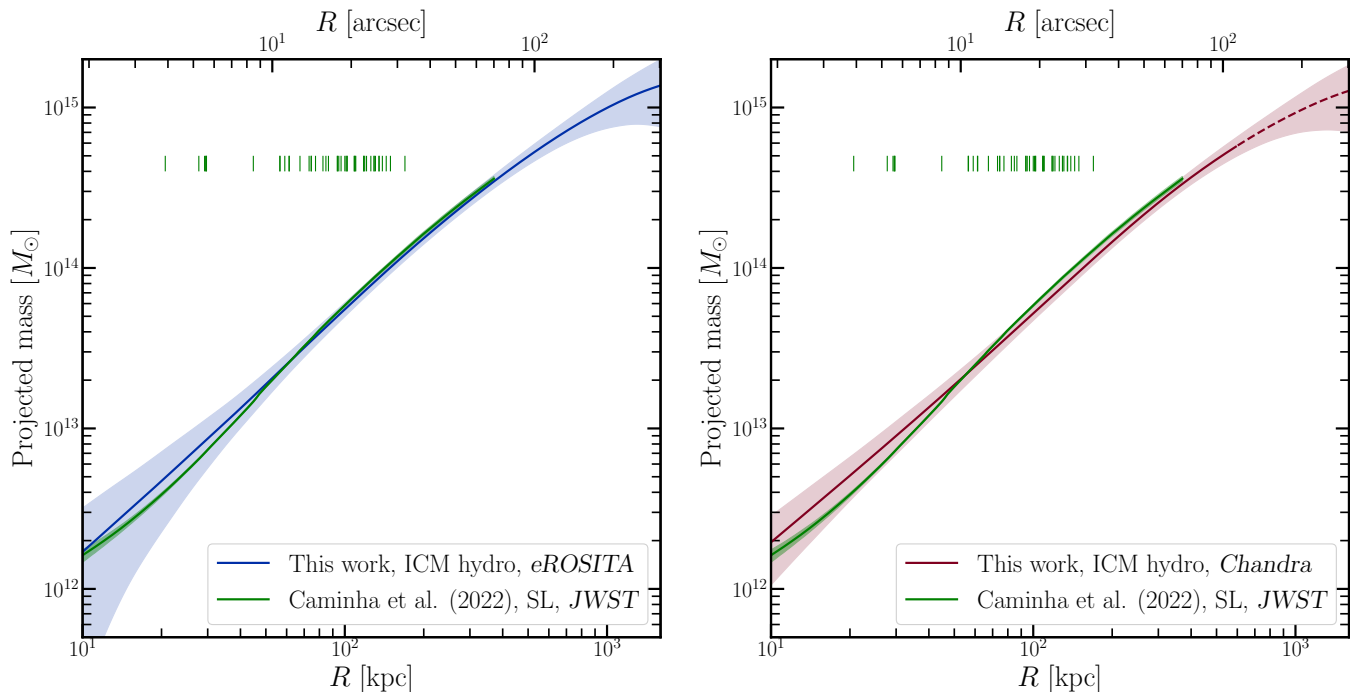
$$M(<r) = -\frac{k_B T r}{G \mu m_p} \left(\frac{d \ln \rho_g}{d \ln r} + \frac{d \ln T}{d \ln r} \right), \quad (3)$$

where k_B is the Boltzmann constant, G is the gravitational constant, $\mu = 0.6$ is the mean atom weight, m_p is proton mass. $\rho_g = n_e m_p A/Z$ is the gas density, where $A \sim 1.4$ and $Z \sim 1.2$ are the average nuclear charge and mass for ICM with 0.3 solar abundance. The uncertainty on the mass profile was computed by randomly picking 2000 samples in the Markov chains of the temperature and density profiles.

The hydrostatic mass profiles measured by *eROSITA* and *Chandra* are plotted in the left panel of Fig. 5. We note that, since we are using the combined temperature profile, the difference in the two profiles results only from the density profiles. We find that the results obtained from *eROSITA* and *Chandra* are in very good agreement, despite the small discrepancies in the very center (< 50 kpc) and the outskirts (> 1 Mpc), which are well within the error bar. From the mass profile measured by *eROSITA* (see the blue line in Fig. 5), we obtained $R_{2500} = 0.54 \pm 0.04$ Mpc, $R_{500} = 1.33 \pm 0.23$ Mpc, and the masses within the two radii $M_{2500} = (3.5 \pm 0.8) \times 10^{14} M_\odot$ and

Table 2. Comparison between *eROSITA* and *Chandra* in the measurements of cluster masses within R_{500} and R_{2500} .

Instrument	R_{500} [Mpc]	$M_{\text{gas},500}$ [$10^{14} M_{\odot}$]	M_{500} [$10^{14} M_{\odot}$]	R_{2500} [Mpc]	$M_{\text{gas},2500}$ [$10^{14} M_{\odot}$]	M_{2500} [$10^{14} M_{\odot}$]
<i>eROSITA</i>	1.33 ± 0.23	1.51 ± 0.02	10.22 ± 5.34	0.54 ± 0.04	0.47 ± 0.01	3.47 ± 0.81
<i>Chandra</i>	1.29 ± 0.21	1.63 ± 0.03	9.15 ± 4.61	0.54 ± 0.04	0.49 ± 0.01	3.36 ± 0.74

**Fig. 6.** Line-of-sight projected mass profiles of J0723 measured by *eROSITA* (left panel) and *Chandra* (right panel). The green curve shows the mass distribution from strong lensing analysis with multiple images discovered by *JWST* (see Fig.A.1 of Caminha et al. 2022). The green bars shows the positions of the multiple images used in the strong lensing analysis.

$M_{500} = (10.2 \pm 5.3) \times 10^{14} M_{\odot}$. The values computed from the *Chandra* results are fully consistent (see Table. 2). The error bars in R_{500} and M_{500} are large, due to the relatively larger uncertainty of the temperature in the outskirts. We also find a perfect agreement with the published results of Lovisari et al. (2020), who measured $M_{500} = 10.10^{+1.57}_{-1.23} \times 10^{14} M_{\odot}$ using the archival data of *XMM-Newton*. The temperature measured by Lovisari et al. (2020), $kT_{500} = 7.53^{+0.53}_{-0.53}$ keV, is slightly lower compared to our temperature profile, but still consistent within 1σ . We also compare the mass of J0723 we measured in this work to the published $L - M$ scaling relation of galaxy clusters. From the luminosity profile measured with MBProj2D using *eROSITA* data, we obtain $L_{500} = 10.73^{+0.14}_{-0.21} \times 10^{44}$ erg/s in the 0.5–2 keV band. Adopting the $L - M$ scaling relation for high redshift and massive clusters in Bulbul et al. (2019), the corresponding mass is $M_{500,\text{SR}} = 10.51^{+0.07}_{-0.11} \times 10^{14} M_{\odot}$, in very good agreement with our results.

With the hydrostatic mass profile and gas mass profile, we also computed the profile of gas mass fraction (f_{gas}), which is shown in the right panel of Fig. 5. With *eROSITA* data, we measure $f_{\text{gas},500} = 0.148^{+0.095}_{-0.038}$ and $f_{\text{gas},2500} = 0.137^{+0.019}_{-0.016}$. From the profile, we observe a clear trend that f_{gas} decreases from 10% in the outskirts (> 1 Mpc) to $< 5\%$ in the core (< 50 kpc), despite that the former has large uncertainty. This is consistent with the

picture that in massive galaxy clusters, the dark matter halo and stellar mass are more concentrated than the hot gas, thus dominating the total mass in the center, while the mass budget tends to be more consistent with the average of the Universe when extending to larger radii (see, e.g., Eckert et al. 2013; Planck Collaboration et al. 2016b).

In order to compare with the strong lensing results, we compute the line-of-sight projected mass using our hydrostatic mass profiles. The projected mass profiles are shown in Fig. 6. We compare our results with the recent strong lensing results published in Caminha et al. (2022), who measure the cluster mass distribution with 46 multiple images from 16 background sources. We find remarkable consistency between the *eROSITA* hydrostatic mass and the strong lensing mass at all radii. At the estimated Einstein radius 128 kpc (Caminha et al. 2022), *eROSITA* measured a projected hydrostatic mass of $(8.1 \pm 0.7) \times 10^{13} M_{\odot}$, in good agreement with the result reported in Caminha et al. (2022): $(8.6 \pm 0.2) \times 10^{13} M_{\odot}$. The measurement of *Chandra* at the same radius: $(7.6 \pm 0.7) \times 10^{13} M_{\odot}$, is only slightly ($\sim 1\sigma$) lower than the strong lensing result, while they tend to be more consistent at larger radii. Using the same *JWST* data, another team measured a strong lensing mass of $(7.6 \pm 0.2) \times 10^{13} M_{\odot}$ at 128 kpc (Mahler et al. 2022), in tension with the result of Caminha et al. (2022) at $\sim 4\sigma$. On the other hand, we note that the

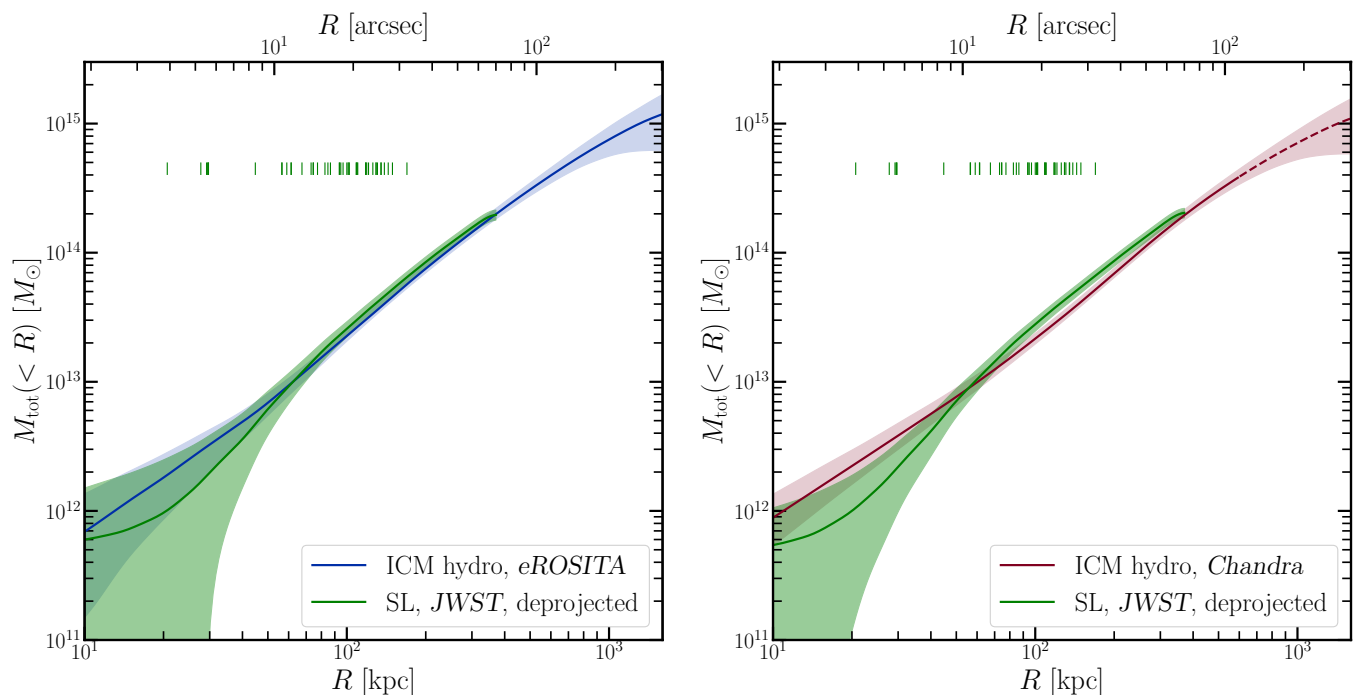


Fig. 7. Comparison between the hydrostatic (hydro) mass profile (blue and red curves) and the strong lensing (SL) mass profile in [Caminha et al. \(2022\)](#) after deprojection (green curves). Left panel is for eROSITA and right panel is for Chandra.

result of [Mahler et al. \(2022\)](#) is consistent with our results for both eROSITA and Chandra within 1σ .

As a further check, we also deproject the strong lensing mass profile from [Caminha et al. \(2022\)](#) using the hydrostatic mass profiles measured by eROSITA and Chandra respectively, and compare it with the hydrostatic mass profiles. From the comparison shown in Fig. 7, the consistency between eROSITA and strong lensing results still remains good. For Chandra, the two profiles are also consistent within $\sim 1\sigma$.

We also remark that, there are many other strong lensing analyzes published in literature, both before and after JWST, thanks to the rapid development of lensing modelization techniques and optical spectroscopic surveys in recent years (e.g., [Fox et al. 2022](#); [Golubchik et al. 2022](#); [Sharon et al. 2022](#)). Despite that most of these works provide consistent results in the center (< 200 kpc), there are tensions at larger radii due to the different tools and data they used. However, here we refrain from comparing our results with all the available strong lensing results, and from discussing the tensions between them, which are beyond the goal of this work.

4. Discussion

In this section, we discuss the systematics and caveats in our analysis. A possible source of bias to our results is the deviation from hydrostatic equilibrium of the ICM in J0723. This deviation can be caused by major/minor mergers (e.g., [Markevitch et al. 2002](#); [Vikhlinin et al. 2001](#)), core sloshing (e.g., [Markevitch et al. 2001](#); [Sanders et al. 2005](#)), gas turbulence (only a few percent, see [Eckert et al. 2019](#)), and other non-gravitational processes such as AGN feedback ([Fabian 2012](#)). On the Chandra image, there are no signs of violent mergers. Weak emission excess is visible ~ 400 kpc to the northeast of the X-ray peak (see the right panel of Fig. 1), possibly associated with a gas

clump, but it is too close to the cluster center and too faint, thus only has negligible impact on the hydrostatic analysis. The offset between the X-ray peak and the position of the brightest cluster galaxy is $\sim 6''$, corresponding to ~ 30 kpc, or $\sim 0.02R_{500}$, implying that J0723 is in a relaxed dynamical status (see, e.g., [Seppi et al. 2021](#)). Moreover, with a visual inspection on the Chandra image, we do not find any significant structure related with AGN mechanical feedback, such as cavities. Although such a visual inspection is limited by the number of photons, and it is hard to quantify the existence/non-existence of cavities, we can conservatively conclude that the impact of feedback is not strong enough to affect our results.

On the Chandra image there is also a mild signal of asymmetry in the central region, which may indicate the sloshing of the core. On the temperature map (see Fig. 3), the coolest region seems to be closer to the west edge of the core, instead of the X-ray peak, which indicates a possible sloshing of the cool core, consistent with the surface brightness image. However, limited by the data quality, we are not able to make further analysis on the dynamical status of the core. In any case, we can confirm that J0723 is well virialised, and the impact of non-hydrostatic gas on the measurement of the hydrostatic mass can be ignored.

5. Conclusions

In this work, we perform X-ray analysis on the galaxy cluster SMACS J0723.3-7327, using the all-sky survey data from the SRG/eROSITA telescope and Chandra observatory. The azimuthally-average profiles of ICM temperature and density are measured with high accuracy from cluster center to the outskirts ($\sim R_{500}$), from which the hydrostatic mass profile is derived. While the high-angular-resolution Chandra data has most of its contribution in measuring the temperature profile in the center, the eROSITA data dominates the constraints from the center to

the outskirts, thanks to the significantly larger effective area (the effective area ratio between *eROSITA* and *Chandra* in 2014 is ~ 10 in the 0.5–2 keV band and ~ 2 in the 2–7 keV band). *eROSITA* and *Chandra* are consistent with each other in the measurements of temperature, density, gas mass, and hydrostatic mass, particularly within $\sim R_{2500}$, while the *Chandra* results in the outskirts are less conclusive due to the shallow observation. The X-ray results are compared with the lens mass model constrained from strong lensing analysis with the latest *JWST* data (Caminha et al. 2022). We find remarkable consistency between the X-ray hydrostatic mass profile and the strong lensing mass distribution at all radii (the latter ends at ~ 400 kpc), both projected and deprojected.

With the published results in the Early Data Release, *eROSITA* has proved its capability particularly in the detection and study of low-mass clusters and groups (see, e.g., Liu et al. 2022; Bulbul et al. 2022; Klein et al. 2022; Bahar et al. 2022; Ghirardini et al. 2022). In this study, we have focused on J0723, a more massive cluster at high redshift ($z = 0.39$) and with high temperature (~ 10 keV). With the eRASS:5 survey depth data, we have measured the X-ray properties of the cluster with comparable accuracy as reached by the same analysis using deeper *Chandra* data. A similarly hot cluster, A3266, has been studied as a calibration target in Sanders et al. (2022), but it is located at a much lower redshift and with a deeper pointing observation. Therefore, with this work, we further verify the capability of *eROSITA*, and also the potential of the all-sky survey data, in the study of massive and distant galaxy clusters.

Acknowledgements. We thank G. B. Caminha for providing the *JWST* strong lensing model. This work is based on data from *eROSITA*, the soft X-ray instrument aboard SRG, a joint Russian-German science mission supported by the Russian Space Agency (Roskosmos), in the interests of the Russian Academy of Sciences represented by its Space Research Institute (IKI), and the Deutsches Zentrum für Luft- und Raumfahrt (DLR). The SRG spacecraft was built by Lavochkin Association (NPOL) and its subcontractors, and is operated by NPOL with support from the Max Planck Institute for Extraterrestrial Physics (MPE). The development and construction of the *eROSITA* X-ray instrument was led by MPE, with contributions from the Dr. Karl Remeis Observatory Bamberg & ECAP (FAU Erlangen-Nuernberg), the University of Hamburg Observatory, the Leibniz Institute for Astrophysics Potsdam (AIP), and the Institute for Astronomy and Astrophysics of the University of Tübingen, with the support of DLR and the Max Planck Society. The Argelander Institute for Astronomy of the University of Bonn and the Ludwig Maximilians Universität Munich also participated in the science preparation for *eROSITA*. The *eROSITA* data shown here were processed using the eSASS/NRTA software system developed by the German *eROSITA* consortium.

A.L. and E.B. acknowledge financial support from the European Research Council (ERC) Consolidator Grant under the European Union’s Horizon 2020 research and innovation programme (grant agreement CoG DarkQuest No 101002585).

References

Arnaud, K. A. 1996, in *Astronomical Society of the Pacific Conference Series*, Vol. 101, *Astronomical Data Analysis Software and Systems V*, ed. G. H. Jacoby & J. Barnes, 17

Asplund, M., Grevesse, N., Sauval, A. J., & Scott, P. 2009, *ARA&A*, 47, 481

Bahar, Y. E., Bulbul, E., Clerc, N., et al. 2022, *A&A*, 661, A7

Bergamini, P., Acebron, A., Grillo, C., et al. 2022, arXiv e-prints, arXiv:2207.09416

Brunner, H., Liu, T., Lamer, G., et al. 2022, *A&A*, 661, A1

Bulbul, E., Chiu, I. N., Mohr, J. J., et al. 2019, *ApJ*, 871, 50

Bulbul, E., Liu, A., Pasini, T., et al. 2022, *A&A*, 661, A10

Bulbul, E., Randall, S. W., Bayliss, M., et al. 2016, *ApJ*, 818, 131

Caminha, G. B., Grillo, C., Rosati, P., et al. 2017, *A&A*, 600, A90

Caminha, G. B., Suyu, S. H., Mercurio, A., et al. 2022, arXiv e-prints, arXiv:2207.07567

Cappellari, M. & Copin, Y. 2003, *MNRAS*, 342, 345

Cash, W. 1979, *ApJ*, 228, 939

Ebeling, H., Edge, A. C., & Henry, J. P. 2001, *ApJ*, 553, 668

Eckert, D., Ettori, S., Molendi, S., Vazza, F., & Paltani, S. 2013, *A&A*, 551, A23

Eckert, D., Ghirardini, V., Ettori, S., et al. 2019, *A&A*, 621, A40

Ettori, S., Donnarumma, A., Pointecouteau, E., et al. 2013, *Space Sci. Rev.*, 177, 119

Ettori, S., Ghirardini, V., Eckert, D., et al. 2019, *A&A*, 621, A39

Ezer, C., Bulbul, E., Nihal Ercan, E., et al. 2017, *ApJ*, 836, 110

Fabian, A. C. 2012, *ARA&A*, 50, 455

Foreman-Mackey, D., Hogg, D. W., Lang, D., & Goodman, J. 2013, *PASP*, 125, 306

Foster, A. R., Ji, L., Smith, R. K., & Brickhouse, N. S. 2012, *ApJ*, 756, 128

Fox, C., Mahler, G., Sharon, K., & Remolina González, J. D. 2022, *ApJ*, 928, 87

Freyberg, M., Perinati, E., Pacaud, F., et al. 2020, in *Society of Photo-Optical Instrumentation Engineers (SPIE) Conference Series*, Vol. 11444, *Society of Photo-Optical Instrumentation Engineers (SPIE) Conference Series*, 114441O

Ghirardini, V., Bahar, Y. E., Bulbul, E., et al. 2022, *A&A*, 661, A12

Ghirardini, V., Ettori, S., Eckert, D., et al. 2018, *A&A*, 614, A7

Girardi, M., Biviano, A., Giuricin, G., Mardirossian, F., & Mezzetti, M. 1993, *ApJ*, 404, 38

Golubchik, M., Furtak, L. J., Meena, A. K., & Zitrin, A. 2022, arXiv e-prints, arXiv:2207.05007

Klein, M., Oguri, M., Mohr, J. J., et al. 2022, *A&A*, 661, A4

Kneib, J.-P. & Natarajan, P. 2011, *A&A Rev.*, 19, 47

Kuntz, K. D. & Snowden, S. L. 2000, *ApJ*, 543, 195

Liu, A., Bulbul, E., Ghirardini, V., et al. 2022, *A&A*, 661, A2

Liu, A., Tozzi, P., Ettori, S., et al. 2020, *A&A*, 637, A58

Liu, A., Tozzi, P., Yu, H., De Grandi, S., & Ettori, S. 2018, *MNRAS*, 481, 361

Lovisari, L., Schellenberger, G., Sereno, M., et al. 2020, *ApJ*, 892, 102

Luo, B., Brandt, W. N., Xue, Y. Q., et al. 2017, *ApJS*, 228, 2

Mahler, G., Jauzac, M., Richard, J., et al. 2022, arXiv e-prints, arXiv:2207.07101

Markevitch, M., Gonzalez, A. H., David, L., et al. 2002, *ApJ*, 567, L27

Markevitch, M., Vikhlinin, A., & Mazzotta, P. 2001, *ApJL*, 562, L153

Mernier, F., Biffi, V., Yamaguchi, H., et al. 2018, *Space Sci. Rev.*, 214, 129

Planck Collaboration, Ade, P. A. R., Aghanim, N., et al. 2016a, *A&A*, 594, A27

Planck Collaboration, Ade, P. A. R., Aghanim, N., et al. 2016b, *A&A*, 594, A13

Planck Collab., Ade, P. A. R., Aghanim, N., et al. 2014, *A&A*, 571, A29

Predehl, P., Andritschke, R., Arefiev, V., et al. 2021, *A&A*, 647, A1

Sanders, J. S., Biffi, V., Brügggen, M., et al. 2022, *A&A*, 661, A36

Sanders, J. S., Fabian, A. C., Russell, H. R., & Walker, S. A. 2018, *MNRAS*, 474, 1065

Sanders, J. S., Fabian, A. C., & Taylor, G. B. 2005, *MNRAS*, 356, 1022

Schellenberger, G., Reiprich, T. H., Lovisari, L., Nevalainen, J., & David, L. 2015, *A&A*, 575, A30

Seppi, R., Comparat, J., Nandra, K., et al. 2021, *A&A*, 652, A155

Sharon, K., Chen, M. C., Mahler, G., Coe, D., & the RELICS Collaboration. 2022, arXiv e-prints, arXiv:2208.08483

Simionescu, A., Werner, N., Mantz, A., Allen, S. W., & Urban, O. 2017, *MNRAS*, 469, 1476

Smith, R. K., Brickhouse, N. S., Liedahl, D. A., & Raymond, J. C. 2001, *ApJ*, 556, L91

Snowden, S. L., Mushotzky, R. F., Kuntz, K. D., & Davis, D. S. 2008, *A&A*, 478, 615

Umetsu, K. 2020, *A&A Rev.*, 28, 7

Vikhlinin, A., Kravtsov, A., Forman, W., et al. 2006, *ApJ*, 640, 691

Vikhlinin, A., Markevitch, M., & Murray, S. S. 2001, *ApJ*, 551, 160

Voges, W., Aschenbach, B., Boller, T., et al. 1999, *A&A*, 349, 389

Willingale, R., Starling, R. L. C., Beardmore, A. P., Tanvir, N. R., & O’Brien, P. T. 2013, *MNRAS*, 431, 394

Wilms, J., Allen, A., & McCray, R. 2000, *ApJ*, 542, 914